

Intensity-only signal-subspace-based imaging

Edwin A. Marengo,* Ronald D. Hernandez, and Hanoch Lev-Ari

Department of Electrical and Computer Engineering, Northeastern University, Boston, Massachusetts 02115, USA

**Corresponding author: emarengo@ece.neu.edu*

Received May 10, 2007; revised September 8, 2007; accepted September 10, 2007;
posted September 24, 2007 (Doc. ID 82916); published October 29, 2007

A signal-subspace method is derived for the localization and imaging of unknown scatterers using intensity-only wave field data (lacking field phase information). The method is an extension of the time-reversal multiple-signal-classification imaging approach to intensity-only data. Of importance, the derived methodology works within exact scattering theory including multiple scattering. © 2007 Optical Society of America

OCIS codes: 100.3190, 100.6640, 290.3200, 070.4340, 070.6020, 110.1650.

1. INTRODUCTION

A computational approach is proposed for wave field intensity-only localization and imaging of unknown scatterers that are embedded in a known homogeneous background medium (as schematically illustrated in Fig. 1). It is assumed that the field data are the intensities of the scattered fields gathered at a receiver aperture or array corresponding to a set of different incident fields that in turn correspond to different illumination aperture or array excitations or “experiments” that we label $t=1, 2, \dots, T$. The problem under study is the estimation (via imaging, e.g.) of the unknown support of the scatterers from the data. Particular attention is given to the special case of M pointlike scatterers whose dimensions are small relative to the probing wavelength(s) and whose internal structure is ignored so that the unknown support is the set of scatterer positions \mathbf{X}_m , $m=1, 2, \dots, M$, but the key ingredients for generalization to extended scatterers whose spatial structure (shape) one wishes to estimate are also developed.

Potential applications that motivate the present research include the localization and imaging of scatterers from intensity-only (phaseless) scattering data for lidar, medical imaging, nondestructive testing of nanomaterials and devices, rough-surface profiling, biological or industrial localization and imaging of pinholes or masks in an opaque screen or, complementarily, of inhomogeneities or impurities in a transparent film, and so on. Motivation is also provided by a number of recent papers [1–5] elucidating the information content of scatterers that is contained in intensity-only (phaseless) scattered field data, along with the associated algorithmic developments, and by earlier work in the general areas of diffraction tomography [6–8] and inverse scattering [9–13] using phaseless field data. Our results complement these and related efforts in intensity-only imaging via a different-signal-subspace point of view. The idea is that despite the lack of field phase information, it is still possible, under certain conditions, to extract the scatterers’ information and, in particular, to arrive at suitable reconstructions from intensity-only data.

The inverse scattering problem with full amplitude and

phase field data is generally nonlinear. Approximations such as that of Born that make the problem linear are applicable only to certain classes of scatterer (e.g., weak scatterers), but more generally the mapping from the scattering potential to the scattered field data is nonlinear as a result of multiple scattering interactions within the object.

A number of iterative optimization approaches have been investigated from time to time to address this nonlinear inverse problem. Yet the search for noniterative schemes for real-time, on-line inversion is of great importance, e.g., in biomedical applications. Also important is the need to better characterize the problem from a theoretical point of view, which requires a formally tractable approach to the problem.

These considerations motivate the modern emphasis of inverse scattering under a more confined, better controlled scope, such as that of reconstructing the scatterers’ support only. In particular, one of the most fruitful areas of modern inverse scattering study is the shape reconstruction or inverse support problem, which is a nonlinear problem tractable under certain conditions via quasi-linearizing approaches. Less restrictive versions of the problem, such as the inversion of both scatterers’ support and scattering potential profile within that support, for special—e.g., piecewise constant scattering potentials—have also been investigated. Of particular interest are noniterative, sampling approaches, sometimes termed “qualitative methods,” that include the linear sampling method, the factorization method, the point-source and singular-source methods, the time-reversal multiple signal classification (MUSIC) method [14–23], and so on (see [24,25] for overviews and references). Of importance, most of these qualitative methods, because of their restricted scope, work within exact scattering theory, including multiple scattering.

Research in this area has emphasized full amplitude and phase data, and thus one naturally wonders whether similar methodologies can be derived also for the intensity-only data case. The present research builds on this particular approach to the problem, and thus our goal is to derive sampling approaches applicable to intensity-

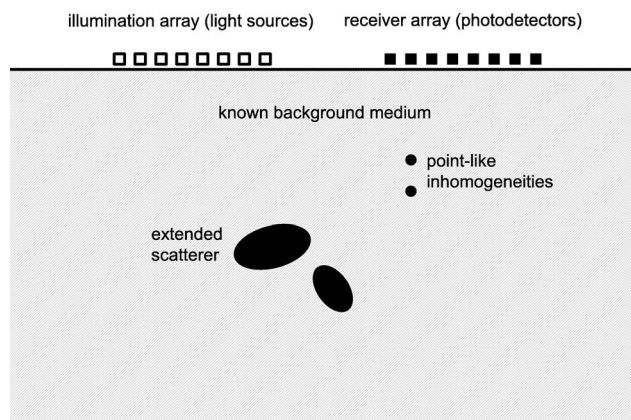


Fig. 1. Schematic of the remote sensing system for intensity-only localization and imaging of pointlike or extended scatterers.

only field data. Like their full-phase-information counterparts [14–25], the derived new sampling approaches may find their way into applications where the scatterer’s shape is of interest, such as certain lidar, biomedical, and nondestructive testing applications. To the best of our knowledge, this particular methodology that may open complementary new avenues in intensity-only imaging has not been established before.

Thus the focus of this paper is the reconstruction of scatterer shapes via sampling imaging methodologies applicable within exact scattering theory, which in the point-target case reduces to target localization. This restricted framework can be seen both as a precursor to subsequent full inverse scattering reconstruction within the thus estimated scatterer’s support and as a method that highlights field information about the scatterer’s support for applications where the scatterer’s shape is of interest.

In the case of full amplitude and phase data, the mapping from the sources induced in the scatterers to the data is linear. This is, in fact, the key behind many of the aforementioned sampling methods (see [23] for an overview of this aspect). But under the more limited intensity-only data, the mapping from the sources induced in the scatterers to the data is nonlinear. In other words, in this case one must cope with an additional nonlinearity, i.e., the mapping from the scattered field to the data (the scattered field intensity measured by the receiver aperture) is quadratic; hence the total mapping from the induced sources to the data is nonlinear. Yet we show next that by considering not the induced sources but instead another source function that still carries the information about the scatterer’s support, the associated mapping becomes (artificially) linearized so that well-known signal subspace approaches for target localization and imaging become readily applicable. In particular, we develop a signal-subspace-based generalization of the so-called time-reversal MUSIC method [14–18] for localization and imaging of scatterers that, unlike previous work in this area, employs intensity-only field data, i.e., without involving field phase information. Of importance, the derived results apply within exact scattering theory; in particular, they do not involve linearizing approximations (e.g., Born approximation) of the mapping from the perti-

nent scattering potential (which depends on the material properties of the scatterers) to the field data.

It is important to point out that time-reversal MUSIC is conceptually similar to the standard MUSIC of statistical signal processing [26,27], as is detailed in [15]. But time-reversal MUSIC uses a pseudo-covariance matrix in place of the true covariance matrix of the original MUSIC approach. Yet time-reversal MUSIC is referred to simply as MUSIC in a number of papers in the target localization and shape reconstruction disciplines [19]. In what follows we adopt this simpler terminology with the understanding that by “MUSIC” we refer to the method developed in the aforementioned papers [14–18] and in some of the references therein and more recent papers [28] including the extended scatterer version of the theory [19–23].

The remainder of the paper is organized as follows. Section 2 addresses the relevant forward-scattering mapping. Section 3 presents the proposed intensity-only signal-subspace-based imaging theory (an “intensity-only MUSIC”) for pointlike scatterers or inhomogeneities. A generalization for extended scatterers is outlined in Section 4 that is based on approximations in essentially finite-dimensional spaces of the governing forward mapping. Unlike the pointlike scatterer framework that enables a rigorous treatment, the extended-scatterer formulation relies on approximations. In Section 5 the proposed methodology for intensity-only signal-subspace-based localization and imaging is illustrated numerically for both the exact pointlike scatterer case and the approximate-extended-scatterer case. Conclusions are given in Section 6.

2. FORWARD RELATIONS

For simplicity of presentation the pertinent developments are given in the framework of the scalar Helmholtz equation that applies to the frequency domain description of scalar fields, but the theory can be readily extended to the full-vector electromagnetic case along obvious lines. To facilitate the discussion of the results, they are presented for homogeneous background media; yet the derived inversion methodology relies mainly on known background Green functions; hence it can be applied to more general nonhomogeneous media as long as the Green function of the background propagating medium is known.

Thus, we consider a homogeneous background medium wherein wave radiation is governed, for scalar sources and fields ρ_t and ψ_t^{inc} , respectively, by the scalar Helmholtz equation

$$(\nabla^2 + k^2)\psi_t^{\text{inc}}(\mathbf{r}) = -\rho_t(\mathbf{r}), \quad (1)$$

where $\mathbf{r} \in R^3$ denotes position, the frequency (ω) dependence has been suppressed, and $k = \omega/c$ (where c is the speed of light in the medium) is the free-space wavenumber of the field at the relevant angular oscillation frequency ω . The fields ψ_t^{inc} correspond to the *incident* fields of the treatment to follow. The label t is employed to denote the t th transmit-plus-receive experiment. It is henceforth assumed that the probing sources ρ_t correspond to an illumination array of N_T radiating point sources located at positions \mathbf{Y}_n , $n = 1, 2, \dots, N_T$ and having excita-

tion strengths $\alpha_{n,t}$, $t=1,2,\dots,T$; $n=1,2,\dots,N_T$, so that they are of the form

$$\rho_t(\mathbf{r}) = \sum_{n=1}^{N_T} \alpha_{n,t} \delta(\mathbf{r} - \mathbf{Y}_n), \quad (2)$$

where δ is Dirac's delta function. The fields ψ_t^{inc} they generate (the incident fields) are of the form

$$\psi_t^{\text{inc}}(\mathbf{r}) = \sum_{n=1}^{N_T} \alpha_{n,t} G(\mathbf{r}, \mathbf{Y}_n), \quad (3)$$

where G denotes the Green function for the Helmholtz operator in Eq. (1) obeying $(\nabla^2 + k^2)G(\mathbf{r}, \mathbf{r}') = -\delta(\mathbf{r} - \mathbf{r}')$ and Sommerfeld's radiation condition, in particular:

$$G(\mathbf{r}, \mathbf{r}') = \frac{\exp(ik|\mathbf{r} - \mathbf{r}'|)}{4\pi|\mathbf{r} - \mathbf{r}'|}. \quad (4)$$

In the presence of the scatterers the total field ψ_t , which is given by the sum of the incident and the scattered field ψ_t^{inc} and ψ_t^{s} , respectively—i.e., $\psi_t = \psi_t^{\text{inc}} + \psi_t^{\text{s}}$ —obeys

$$(\nabla^2 + k^2)\psi_t(\mathbf{r}) = V(\mathbf{r})\psi_t(\mathbf{r}) - \rho_t(\mathbf{r}), \quad (5)$$

where the scattering potential function $V(\mathbf{r}) = k^2 - K^2(\mathbf{r})$, where in turn $K(\mathbf{r})$ is the space-dependent wavenumber of the field in the total (background plus scatterers) medium.

It now follows from Eqs. (1) and (5) and standard manipulations involving Green's theorem and Sommerfeld's radiation condition for the scattered fields that the field ψ_t^{s} scattered by an unknown scatterer of support D (so that its scattering potential V is of support D) when excited by an incident field ψ_t^{inc} can be expressed as [29–31]

$$\psi_t^{\text{s}}(\mathbf{r}) = \int d\mathbf{r}' G(\mathbf{r}, \mathbf{r}') I_D(\mathbf{r}') Q_t(\mathbf{r}'), \quad (6)$$

where Q_t represents the source induced over the scatterer due to excitation with probing field ψ_t^{inc} , and $I_D(\mathbf{r})$ is a masking or indicator function whose value is defined as $I_D(\mathbf{r}) = 1$ if $\mathbf{r} \in D$ and $I_D(\mathbf{r}) = 0$ otherwise. Now, the induced source Q_t in these developments is given within exact scattering theory (including multiple scattering) by [29–31]

$$Q_t(\mathbf{r}) = V(\mathbf{r})[(I - \widetilde{GV})^{-1}\psi_t^{\text{inc}}](\mathbf{r}), \quad (7)$$

where I is the identity operator and the linear mapping \widetilde{GV} is defined by

$$(\widetilde{GV}\psi_t)(\mathbf{r}) = \int d\mathbf{r}' G(\mathbf{r}, \mathbf{r}') V(\mathbf{r}') \psi_t(\mathbf{r}'). \quad (8)$$

It follows from Eq. (6) that the intensity $I_t(\mathbf{r})$ of the scattered field $\psi_t^{\text{s}}(\mathbf{r})$ is given by

$$I_t(\mathbf{r}) = |\psi_t^{\text{s}}(\mathbf{r})|^2 = \int d\mathbf{r}' \int d\mathbf{r}'' \mathcal{H}(\mathbf{r}; \mathbf{r}', \mathbf{r}'') Q_t(\mathbf{r}', \mathbf{r}''), \quad (9)$$

where the kernel

$$\mathcal{H}(\mathbf{r}; \mathbf{r}', \mathbf{r}'') = G^*(\mathbf{r}, \mathbf{r}') G(\mathbf{r}, \mathbf{r}'') I_D(\mathbf{r}') I_D(\mathbf{r}'') \quad (10)$$

(where $*$ denotes complex conjugation) depends only on the known background Green function and the sought after scatterer support D , and where we have introduced the new source function term

$$Q_t(\mathbf{r}', \mathbf{r}'') = Q_t^*(\mathbf{r}') Q_t(\mathbf{r}''). \quad (11)$$

An alternative and insightful form of Eq. (9) is found by noting that expressions (10) and (11) imply $\mathcal{H}(\mathbf{r}; \mathbf{r}', \mathbf{r}'') = \mathcal{H}^*(\mathbf{r}; \mathbf{r}'', \mathbf{r}')$ and $Q_t(\mathbf{r}', \mathbf{r}'') = Q_t^*(\mathbf{r}'', \mathbf{r}')$ so that Eq. (9) can be written as

$$\begin{aligned} I_t(\mathbf{r}) &= \int d\mathbf{r}' \mathcal{H}(\mathbf{r}; \mathbf{r}', \mathbf{r}') Q_t(\mathbf{r}', \mathbf{r}') \\ &+ 2\Re \left[\int d\mathbf{r}' \int_{\{x'' < x', y'' < y', z'' < z'\}} d\mathbf{r}'' \mathcal{H}(\mathbf{r}; \mathbf{r}', \mathbf{r}'') Q_t(\mathbf{r}', \mathbf{r}'') \right] \\ &= \int d\mathbf{r}' \mathcal{H}(\mathbf{r}; \mathbf{r}', \mathbf{r}') Q_t(\mathbf{r}', \mathbf{r}') \\ &+ 2 \int d\mathbf{r}' \int_{\{x'' < x', y'' < y', z'' < z'\}} \\ &\quad \times d\mathbf{r}'' \Re[\mathcal{H}(\mathbf{r}; \mathbf{r}', \mathbf{r}'')] \Re[Q_t(\mathbf{r}', \mathbf{r}'')] \\ &- 2 \int d\mathbf{r}' \int_{\{x'' < x', y'' < y', z'' < z'\}} \\ &\quad d\mathbf{r}'' \Im[\mathcal{H}(\mathbf{r}; \mathbf{r}', \mathbf{r}'')] \Im[Q_t(\mathbf{r}', \mathbf{r}'')], \end{aligned} \quad (12)$$

where \Re and \Im denote the real and imaginary parts, respectively, while (x', y', z') and (x'', y'', z'') are the Cartesian coordinate representations of \mathbf{r}' and \mathbf{r}'' , respectively. It is convenient to further compress Eq. (12) by noting that $\Re[\mathcal{H}(\mathbf{r}; \mathbf{r}', \mathbf{r}'')] = \mathcal{H}(\mathbf{r}; \mathbf{r}', \mathbf{r}'')$ and $\Re[Q_t(\mathbf{r}', \mathbf{r}'')] = Q_t(\mathbf{r}', \mathbf{r}'')$ [these results follow from the facts $\mathcal{H}(\mathbf{r}; \mathbf{r}', \mathbf{r}'') = \mathcal{H}^*(\mathbf{r}; \mathbf{r}'', \mathbf{r}')$ and $Q_t(\mathbf{r}', \mathbf{r}'') = Q_t^*(\mathbf{r}'', \mathbf{r}')$ noted earlier] so that by introducing

$$\bar{\mathcal{H}}(\mathbf{r}; \mathbf{r}', \mathbf{r}'', j) = \begin{cases} \Re[\mathcal{H}(\mathbf{r}; \mathbf{r}', \mathbf{r}'')] & j = 1 \\ \Im[\mathcal{H}(\mathbf{r}; \mathbf{r}', \mathbf{r}'')] & j = 2 \end{cases} \quad (13)$$

and

$$\bar{Q}_t(\mathbf{r}', \mathbf{r}'', j) = \begin{cases} 2\Re[Q_t(\mathbf{r}', \mathbf{r}'')] [1 - \frac{1}{2}\delta(\mathbf{r}' - \mathbf{r}'')] & j = 1 \\ -2\Im[Q_t(\mathbf{r}', \mathbf{r}'')] & j = 2 \end{cases} \quad (14)$$

Eq. (12) can be expressed as

$$\begin{aligned} I_t(\mathbf{r}) &= \int d\mathbf{r}' \int_{\{x'' \leq x', y'' \leq y', z'' \leq z'\}} d\mathbf{r}'' \bar{\mathcal{H}}(\mathbf{r}; \mathbf{r}', \mathbf{r}'', 1) \bar{Q}_t(\mathbf{r}', \mathbf{r}'', 1) \\ &+ \int d\mathbf{r}' \int_{\{x'' < x', y'' < y', z'' < z'\}} d\mathbf{r}'' \bar{\mathcal{H}}(\mathbf{r}; \mathbf{r}', \mathbf{r}'', 2) \bar{Q}_t(\mathbf{r}', \mathbf{r}'', 2), \end{aligned} \quad (15)$$

which is more eloquent than Eq. (12) in the language of signal-subspace methods, as will become clear later.

Our focus in this work is the inverse or imaging aspect. Specifically, a MUSIC-like signal-subspace-based imaging

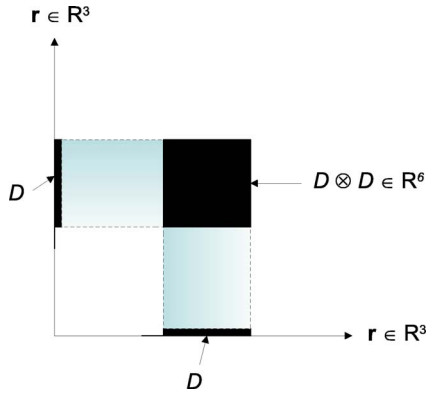


Fig. 2. (Color online) Conceptual depiction of the support regions D and $D \otimes D$ in R^3 and R^6 spaces, respectively.

method is sought for the estimation of the unknown scatterer support D from knowledge of the scattered intensity I_t due to a number of transmit experiments or sources $\rho_t, t=1, 2, \dots, T$ and measured at a number of receiver

points $\mathbf{Z}_n, n=1, 2, \dots, N_R$, which corresponds to a total of TN_R measured field intensities $I_t(\mathbf{Z}_n), t=1, 2, \dots, T; n=1, 2, \dots, N_R$. For each t , one then measures the $N_R \times 1$ intensity vector

$$\mathbf{I}_t = [I_t(\mathbf{Z}_1), I_t(\mathbf{Z}_2), \dots, I_t(\mathbf{Z}_{N_R})] \in R^{N_R}. \quad (16)$$

At this point, it is formally convenient to introduce the linear mapping $P: \mathcal{X} \rightarrow \mathcal{Y}$, where \mathcal{X} is the Hilbert space of square-integrable real-valued source functions \bar{Q}_t of $(\mathbf{r}', \mathbf{r}'', j) \in R^6 \otimes \{1, 2\}$, where \otimes denotes the Cartesian product—whose support in $R^6 \otimes \{1, 2\}$ is $D \otimes D \otimes \{1, 2\}$ (for a schematization of the support $D \otimes D$ in R^6 refer to Fig. 2)—and for which we define the weighted inner product

$$\langle \bar{Q}_t | \bar{Q}'_t \rangle_{\mathcal{X}} = \sum_{j=1}^2 \int d\mathbf{r}' \int d\mathbf{r}'' w(\mathbf{r}', \mathbf{r}'', j) \bar{Q}_t(\mathbf{r}', \mathbf{r}'', j) \bar{Q}'_t(\mathbf{r}', \mathbf{r}'', j), \quad (17)$$

where the weighting function

$$w(\mathbf{r}', \mathbf{r}'', j) = \begin{cases} 1 & \text{if } (\mathbf{r}', \mathbf{r}'', j) \in D \otimes [D \cap \{x'' \leq x', y'' \leq y', z'' \leq z'\}] \otimes \{1\} \\ 1 & \text{if } (\mathbf{r}', \mathbf{r}'', j) \in D \otimes [D \cap \{x'' < x', y'' < y', z'' < z'\}] \otimes \{2\}, \\ 0 & \text{otherwise} \end{cases} \quad (18)$$

and where \mathcal{Y} is the data space of real-valued N_R -tuples to which we assign the inner product defined by

$$\langle \mathbf{I}_t | \mathbf{I}'_t \rangle_{\mathcal{Y}} = \sum_{n=1}^{N_R} \mathbf{I}_t(n) \mathbf{I}'_t(n). \quad (19)$$

According to Eqs. (15), (16), and (18) this linear mapping is defined such that

$$\begin{aligned} \mathbf{I}_t(n) &= (P \bar{Q}_t)(n) \\ &= \sum_{j=1}^2 \int d\mathbf{r}' \int d\mathbf{r}'' w(\mathbf{r}', \mathbf{r}'', j) \bar{H}(\mathbf{Z}_n; \mathbf{r}', \mathbf{r}'', j) \bar{Q}_t(\mathbf{r}', \mathbf{r}'', j) \\ n &= 1, 2, \dots, N_R. \end{aligned} \quad (20)$$

Having arrived at this formality, we wish to divide for pedagogical reasons the following discussion into two cases, namely, a general case to be handled approximately, and a particular case that can be solved exactly:

1. General case of an extended scatterer of support D . This case will be discussed using well-known properties of the singular-value decomposition (SVD) of the compact linear mapping P defined in Eq. (20) that will facilitate approximations leading to the approximate imaging of the sought-after scatterer from intensity-only data. The proposed imaging is outlined in Section 4 and accounts for a new support inversion or shape reconstruction method with intensity-only data.

2. Special case of a total scatterer composed of a collection of small scatterers which for the given wavelength can be modelled as point targets so that the sought-after

support is of the form $D = \{\mathbf{X}_1, \mathbf{X}_2, \dots, \mathbf{X}_M\}$ where $\mathbf{X}_m, m=1, 2, \dots, M$ are the target locations. This case will be considered without approximations in the next section, and, in particular, conditions enabling perfect localization of the targets in the absence of noise will be given. The effect of noise in the data will be considered numerically in section 5.

The key forward relation for the remainder of the paper is Eq. (20). For the special case of M point scatterers at positions $\mathbf{X}_m, m=1, 2, \dots, M$ this result can be readily seen to take the particular form

$$\begin{aligned} \mathbf{I}_t(n) &= (P \bar{Q}_t)(n) = \sum_{m=1}^M \sum_{m' \leq m} \bar{H}(\mathbf{Z}_n; \mathbf{X}_m, \mathbf{X}_{m'}, 1) \bar{Q}_t(\mathbf{X}_m, \mathbf{X}_{m'}, 1) \\ &+ \sum_{m=1}^M \sum_{m' < m} \bar{H}(\mathbf{Z}_n; \mathbf{X}_m, \mathbf{X}_{m'}, 2) \bar{Q}_t(\mathbf{X}_m, \mathbf{X}_{m'}, 2) \end{aligned} \quad (21)$$

where $n=1, 2, \dots, N_R$. Section 3 investigates intensity-only signal-subspace-based localization of the M point scatterers under the signal model of Eq. (21).

3. INTENSITY-ONLY SIGNAL-SUBSPACE-BASED IMAGING OF POINTLIKE SCATTERERS

Consider the $N_R \times 1$ propagator vectors $\mathbf{U}^{(\mathbf{R}, \mathbf{R}')} and $\mathbf{V}^{(\mathbf{R}, \mathbf{R}'}$ defined by$

$$\mathbf{U}^{(\mathbf{R}, \mathbf{R}')} (n) = \Re[G^*(\mathbf{Z}_n, \mathbf{R})G(\mathbf{Z}_n, \mathbf{R}')],$$

$$\mathbf{V}^{(\mathbf{R}, \mathbf{R}')} (n) = \Im[G^*(\mathbf{Z}_n, \mathbf{R})G(\mathbf{Z}_n, \mathbf{R}')] \quad n = 1, 2, \dots, N_R. \quad (22)$$

Using Eqs. (10), (13), and (22) one finds that Eq. (21) can be expressed as

$$\begin{aligned} \mathbf{I}_t = P\bar{Q}_t &= \sum_{m=1}^M \sum_{m' \leq m} \bar{Q}_t(\mathbf{X}_m, \mathbf{X}_{m'}, 1) \mathbf{U}^{(\mathbf{X}_m, \mathbf{X}_{m'})} \\ &+ \sum_{m=1}^M \sum_{m' \leq m} \bar{Q}_t(\mathbf{X}_m, \mathbf{X}_{m'}, 2) \mathbf{V}^{(\mathbf{X}_m, \mathbf{X}_{m'})}, \end{aligned} \quad (23)$$

where without loss of generality we have included the case $m=m'$ in the second summation since $\mathbf{V}^{(\mathbf{X}_m, \mathbf{X}_m)} = 0$. This expression points up that the data vectors \mathbf{I}_t , $t=1, 2, \dots, T$ lie in (and that P maps into) the signal space

$$\mathcal{S}_y = \text{Span}[\mathbf{U}^{(\mathbf{X}_m, \mathbf{X}_{m'})}, \mathbf{V}^{(\mathbf{X}_m, \mathbf{X}_{m'})},$$

$$m = 1, 2, \dots, M; \quad m' \leq m,$$

where \mathbf{X}_m , $m=1, 2, \dots, M$ are the sought-after scatterer positions.

Assuming a number of photodetectors $N_R > M^2$, this space can be shown from the results and methodology in [28,32] to be of dimensionality M^2 under mild conditions. Thus if one carries out sufficiently many experiments (T is sufficiently large) as to let the data vectors fully span the signal space or range of the linear map P , then the rank of the $N_R \times T$ data matrix $[\mathbf{I}_1 \mathbf{I}_2 \dots \mathbf{I}_T]$ is M^2 (under low additive noise this becomes an “effective”, or numerical, rank). Furthermore, the SVD of the data matrix will reveal signal subspace vectors W_p , $p=1, 2, \dots, M^2$ having nonzero singular values σ_p and defining the range of the mapping P or the signal subspace $\mathcal{S}_y = \text{Span}(W_p, p \leq M^2)$.

Similarly, the SVD of the data matrix will reveal noise subspace vectors W_p , $p=M^2+1, M^2+2, \dots, N_R$ spanning the orthogonal complement of \mathcal{S}_y in \mathcal{Y} , that is, the noise subspace $\mathcal{S}_y^\perp = \text{Span}(W_p, p > M^2)$. This information, that is, the signal subspace data vectors W_p , $p \leq M^2$ and the complementary noise subspace vectors W_p , $p > M^2$ that can be deduced from the measured data, is the basis for the localization method given next. Thus, once the data are gathered and the signal subspace and noise subspace vectors have been determined from the data, one can obtain images of the scatterers pinpointing their locations by plotting the following pseudospectra versus position in a given region of search or of interest where the targets are being sought.

Two variants of the approach are possible. One is computationally intensive and requires exhaustive search in six-dimensional space R^6 , which can be implemented numerically using genetic algorithms [28]. The other approach is much less intensive and requires search in three-dimensional space R^3 .

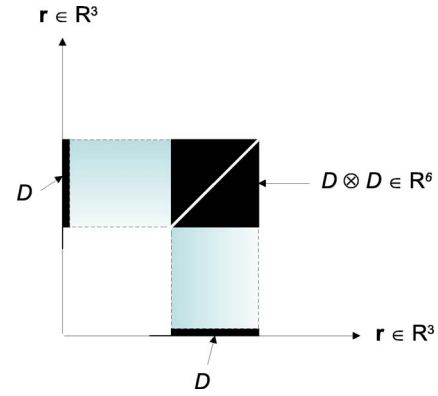


Fig. 3. (Color online) Indicated diagonal line dividing the support region $D \otimes D$ in R^6 corresponds to the subset of that support that is associated with the points $(\mathbf{R}, \mathbf{R}') \in R^6$ and their propagators $\mathbf{U}^{(\mathbf{R}, \mathbf{R}')}$ used in the noncomputationally intensive version of the intensity-only signal-subspace-based imaging algorithm of this work.

The computationally intensive version is as follows. Since

$$\mathcal{S}_y = \text{Span}[\mathbf{U}^{(\mathbf{X}_m, \mathbf{X}_{m'})}, \mathbf{V}^{(\mathbf{X}_m, \mathbf{X}_{m'})},$$

$$m = 1, 2, \dots, M; \quad m' \leq m,$$

and also $\mathcal{S}_y = \text{Span}(W_p, p \leq M^2)$ while $\mathcal{S}_y^\perp = \text{Span}(W_p, p > M^2)$, then if $(\mathbf{R}, \mathbf{R}')$ coincides with any of the combinations $(\mathbf{X}_m, \mathbf{X}_{m'})$, $m=1, 2, \dots, M$; $m'=1, 2, \dots, M$, then the vectors $\mathbf{U}^{(\mathbf{R}, \mathbf{R}')}$ and $\mathbf{V}^{(\mathbf{R}, \mathbf{R}')}$ introduced in Eq. (22) are orthogonal to the noise subspace \mathcal{S}_y^\perp . Therefore, the pseudospectrum

$$A(\mathbf{R}, \mathbf{R}') = \left[\sum_{p > M^2} |\langle W_p | \mathbf{U}^{(\mathbf{R}, \mathbf{R}')} \rangle_{\mathcal{Y}}|^2 + \sum_{p > M^2} |\langle W_p | \mathbf{V}^{(\mathbf{R}, \mathbf{R}')} \rangle_{\mathcal{Y}}|^2 \right]^{-1} \quad (24)$$

peaks to infinity for the correct test two-point selections $(\mathbf{R}, \mathbf{R}') \in \{(\mathbf{X}_m, \mathbf{X}_{m'}), m=1, 2, \dots, M; m'=1, 2, \dots, M\}$ and has finite value for noncorrect two-point selections, which provides the basis for the proposed scatterer localization methodology. Thus, for imaging, one can plot, the projected pseudospectrum versus \mathbf{R} :

$$A_p(\mathbf{R}) = \max_{\mathbf{R}'} [A(\mathbf{R}, \mathbf{R}')], \quad (25)$$

where $\max_{\mathbf{R}'} [A(\mathbf{R}, \mathbf{R}')]$, which is a function of \mathbf{R} only, is computed by fixing the given \mathbf{R} and taking the maximum value of the resulting quantity $A(\mathbf{R}, \mathbf{R}')$ over all values of \mathbf{R}' , and which will have large values for test points in and near the correct two-point selections corresponding to the correct scatterer positions.

The noncomputationally intensive version of the method uses Eq. (24) only for $\mathbf{R}=\mathbf{R}'$. This reduces the dimensionality of the search space from six to three. In particular, the respective pseudospectrum is $A(\mathbf{R}, \mathbf{R})$ (refer to Fig. 3). The image of the scatterer is obtained by plotting this pseudospectrum versus \mathbf{R} , which will reveal peaks for the correct selections $\mathbf{R}=\mathbf{X}_m$, $m=1, 2, \dots, M$.

4. INTENSITY-ONLY SIGNAL-SUBSPACE-BASED IMAGING OF EXTENDED SCATTERERS

The following method for extended scatterers whose structure or shape one wishes to estimate is based on signal subspace concepts and, in particular, relies on the SVD of the linear mapping P defined by Eq. (20), which is of the form [33]

$$(P\bar{Q}_t)(n) = \sum_{p=1}^{N_R} \sigma_p W_p(n) \langle \mathcal{R}_p | \bar{Q}_t \rangle_{\mathcal{X}}, \quad (26)$$

where $(\sigma_p, \mathcal{R}_p, W_p)$, $p=1, 2, \dots, N_R$, constitutes the singular system of P : σ_p are the relevant singular values, and $\mathcal{R}_p \in \mathcal{X}$ and $W_p \in \mathcal{Y}$ are the associated right-hand singular functions and left-hand singular vectors, respectively. In the extended scatterer case, the number of strictly non-zero singular values σ_p of the linear mapping P is N_R . Thus, unlike in the noise-free signal model for point targets wherein P can have a *true null subspace* of singular functions having strictly zero singular value, as we explained earlier, in the present extended scatterer case this is not the case (strictly speaking, there is *no null subspace* in this case), and one must rely on approximations, as we elaborate in the following.

The approximations in question provide a quasi-signal subspace of nonsmall singular values as well as a complementary quasi-noise subspace of very small singular values that one can handle numerically in a way similar to the true null or noise subspace of the respective pointlike scatterer theory. The question of selecting an optimal cutoff for the singular value index separating quasi-signal versus quasi-noise subspaces is a topic that belongs to regularization theory and to the approximation of compact operators in essentially finite dimensional spaces (see [21,34–37]; see also the discussion on number of degrees of freedom of linear operators and on the related selection of the signal-versus-noise cutoff in [23] and the recent account on ε -approximation of compact linear mappings for time-reversal MUSIC imaging of extended targets in [38]).

In the computer simulations associated with this work we successfully implemented the basic approach of estimating the cutoff from the “knee” of the singular value spectrum as given in log-scale. As addressed in a previous paper [23] on the associated “with phase” time-reversal MUSIC imaging of extended targets, this method is approximately equivalent in practice to the standard L -curve-based approach of ill-posed inverse problems [33], which in the present imaging context takes two forms, *a priori* and *a posteriori* L curves as detailed in [23] (pp. 1977–1979).

In particular, it is possible that, for sufficiently large N_R , a certain saturation can be reached so the singular values σ_p decay exponentially fast for some $p > L$, so that $\sigma_p \approx 0$ for $p > L$, where $L < N_R$ is the effective number of degrees of freedom or dimensions of the field data [34,35]. This situation is well known [33,36], e.g., it is standard in the theory of compact linear mappings, and is the basis for the ill-posedness of the inverse problem. The condition $L < N_R$ is also the basis for the MUSIC-like imaging approach that follows, which is formalized by introducing

the L -dimensional subspace $S_y \subset \mathcal{Y}$ of \mathcal{Y} which is spanned by the principal field functions $W_p, p \leq L$ having non-negligible singular values σ_p as well as its $(N_R - L)$ -dimensional orthogonal complement S_y^\perp in \mathcal{Y} , which in turn is spanned by the field functions $W_p, p > L$ having negligible singular values σ_p .

Most of the information about the scatterer that can be reliably extracted from the available data is contained in the L -dimensional signal subspace S_y ; in fact, essentially all the data lie in this subspace, thereby having almost zero projection to the respective $(N_R - L)$ -dimensional orthogonal complement S_y^\perp . If a method can be thought of to deduce from the data this signal subspace S_y , and along with it, its associated (and nonempty) complement S_y^\perp —both of which according to the definition of the mapping P [Eqs. (10), (18), and (20)] must depend only on the known Green function G and the unknown support D , thereby being completely independent of the details of the material structure of the scatterer (e.g., interior index of refraction)—then an approach similar to MUSIC can be used for the determination of the scatterer support that is applicable under mild conditions to spatially extended objects.

In this context we rewrite Eqs. (20) and (26) as

$$\mathbf{I}_t = P\bar{Q}_t \approx \sum_{p=1}^L \sigma_p W_p \langle \mathcal{R}_p | \bar{Q}_t \rangle_{\mathcal{X}} \quad (27)$$

where we have approximated P by a truncation of its singular system representation Eq. (26) so as to include only the respective “principal components” of the data. We see from relation (27) that for any experiment (t), the scattered field intensity vector \mathbf{I}_t can be approximated as a signal in the signal subspace $S_y \equiv \text{Span}(W_p, p \leq L)$. Then, for sufficiently large number T of experiments, the subspace of \mathcal{Y} spanned by the measured intensities $\mathbf{I}_t [t=1, 2, \dots, T]$, i.e., $\text{Span}(\mathbf{I}_t, t=1, 2, \dots, T)$, essentially coincides with the M -dimensional signal subspace S_y , thereby also revealing the associated $(N_R - L)$ -dimensional orthogonal complement or null subspace S_y^\perp . From this one can deduce, if this complement is nonempty, i.e., if $L < N_R$, the scatterer support via the following MUSIC-like procedure. In particular, after one gathers the data vectors $\mathbf{I}_t, t=1, 2, \dots, T$, one can arrange them as the $N_R \times T$ data matrix $[\mathbf{I}_1 \mathbf{I}_2 \dots \mathbf{I}_T]$ and deduce (via standard SVD or principal component analysis of this data matrix) the effective rank L , the principal or signal subspace data vectors $W_p, p \leq L$, and the noise subspace vectors $W_p, p > L$. Finally, one can obtain images of the scatterer based on the pseudospectra discussed next. Again, we emphasize that unlike the pointlike scatterer theory, where there can be true signal and null subspaces under the conditions stated in the previous analysis, in the present extended-target case whenever we refer to signal and noise subspaces what is meant is quasi-signal and quasi-noise subspaces determined by a practical selection of a cutoff singular value index that can be done, e.g., from estimation of the knee in the log-scale singular-value spectrum of the data matrix or by the L -curve methods in [23].

As in the case of pointlike scatterer inversion, two variants of the method are possible. One is computationally

intensive and requires exhaustive search in six-dimensional space R^6 . The other approach is much less intensive, requiring search in three-dimensional space R^3 .

The computationally intensive version is as follows. Returning to relations (10), (13), (18), and (20) we note that P maps into the space spanned by the $N_R \times 1$ propagator vectors $\mathbf{U}^{(\mathbf{R}, \mathbf{R}')}$ and $\mathbf{V}^{(\mathbf{R}, \mathbf{R}')}$ defined by Eqs. (22), where $(\mathbf{R}, \mathbf{R}') \in D \otimes [D \cap \{x' \leq x, y' \leq y, z' \leq z\}]$. Thus the vectors in Eqs. (22) corresponding to $(\mathbf{R}, \mathbf{R}') \in D \otimes D$ are in the data space while the vectors in Eqs. (22) for $(\mathbf{R}, \mathbf{R}') \notin D \otimes D$ are not in the data space. Within computational accuracy (i.e., essentially), the vectors in Eq. (22) corresponding to $(\mathbf{R}, \mathbf{R}') \in D \otimes D$ have large projections into the effective signal subspace \mathcal{S}_y , while they have small projections into the orthogonal complement \mathcal{S}_y^\perp . On the contrary, essentially the vectors in Eqs. (22) corresponding to $(\mathbf{R}, \mathbf{R}') \notin D \otimes D$ have small projections into the effective signal subspace \mathcal{S}_y , while they have large projections into the orthogonal complement \mathcal{S}_y^\perp . Then the high-dimensional pseudospectrum

$$A(\mathbf{R}, \mathbf{R}') = \left[\sum_{p>L} |\langle W_p | \mathbf{U}^{(\mathbf{R}, \mathbf{R}')} \rangle_y|^2 + \sum_{p>L} |\langle W_p | \mathbf{V}^{(\mathbf{R}, \mathbf{R}')} \rangle_y|^2 \right]^{-1} \quad (28)$$

peaks (has large value) for test two-point selections $(\mathbf{R}, \mathbf{R}')$ in and near the sought-after support $D \otimes D$, i.e., $(\mathbf{R}, \mathbf{R}') \in D \otimes D$. For imaging, one can plot the projected pseudospectrum

$$A_p(\mathbf{R}) = \max_{\mathbf{R}'} [A(\mathbf{R}, \mathbf{R}')] \quad (29)$$

versus \mathbf{R}' that will have high values in and around the sought-after scatterer support D . This completes the approach to highlight the sought-after scatterer support D presumably with good results under low noise.

The less intensive method uses Eq. (28) only for $\mathbf{R} = \mathbf{R}'$, which reduces the dimensionality of the search space from six to three, in particular, the respective pseudospectrum is $A(\mathbf{R}, \mathbf{R})$ (refer to Fig. 3). The image of the scatterer is obtained by plotting this pseudospectrum versus \mathbf{R} .

5. COMPUTER ILLUSTRATIONS

To illustrate, we consider next the basic problem of interrogation in three-dimensional free space of two pointlike scatterers ($M=2$) by a square array of $11 \times 11 = 121$ one-wavelength-separated point transmitters (point sources) and receivers (photodetectors) (thus $N_T=121$ and $N_R=121$). The geometry of the problem is shown in Fig. 4 where all dimensions are given in the scale of the wavelength $\lambda = 2\pi/k$. The background Green function $G(\mathbf{r}, \mathbf{r}')$ is then given by Eq. (4) where $k=2\pi/\lambda$, and in the simulations we take the wavelength $\lambda=1$. The familiar Foldy-Lax multiple-scattering model [e.g., [39], Eqs. (7) and (8); [40], Eqs. (3.7) and (3.8); [41], pp. 246–248; [42], pp. 376–382; [43], Eqs. (14-7a) and (14-7b); [44], Eqs. 1 and 2; [18], Eq. 2] is adopted in carrying out the associated forward-scattering computations so as to simulate multiple scattering between the scatterers.

For the experiments, we set the target scattering strengths $\tau_1 = \tau_2 = 1$. Thus we take $V(\mathbf{r}) = \tau_1 \delta(\mathbf{r} - \mathbf{X}_1) + \tau_2 \delta(\mathbf{r} - \mathbf{X}_2)$, and the goal is to deduce the unknown point scatterers' positions \mathbf{X}_1 and \mathbf{X}_2 from intensity-only scattered field data as gathered by transmit-plus-receive experiments based on the array. The adopted configuration is meant to simulate a so-called limited-view configuration, wherein the sources for interrogation and the receivers for measurement are confined to a given limited-view region that does not fully enclose the scatterers.

As transmit experiments, we select a given point source as transmit experiment, thus a total of 121 transmit experiments are implemented, and for each experiment we gather the scattered-field-intensity vector as seen at the receiving aperture [it is thus assumed that the incident fields can be filtered out, e.g., by time gating, the use of Mach-Zehnder interferometry to separate incident and scattered fields, or other approaches (e.g., [9,10]), so that we can obtain the scattered-field-intensity vector as data for the algorithms].

As shown in Fig. 4, in our first set of simulation experiments we set the point scatterers at positions $\mathbf{X}_1 = (X_1, Y_1, Z_1) = (2, 5, 0)$ and $\mathbf{X}_2 = (X_2, Y_2, Z_2) = (8, 5, 0)$, while the probing aperture is located at the plane defined by $Z=15$, so that the target separation is 6λ while the separation between the target and aperture planes is 15λ . For this particular geometry, we explore both the computationally intensive and the noncomputationally intensive versions of the method discussed in Eqs. (24) and (25). The following results illustrate, for this example, the imaging via Eqs. (24) and (25) of the scatterers under noise-free conditions as well as under 20 dB signal-to-noise ratio (SNR) determined as in [23]. Comparative results shedding light on the resolution ability of the intensity-and-phase versus the intensity-only cases, where the latter involves the two variants (intensive versus nonintensive), are also discussed.

In the first set of simulations, noise-free data were used to estimate the scatterer positions \mathbf{X}_m , $m=1,2$ with encouraging results. Figure 5 illustrates the respective pseudospectrum image $A(\mathbf{R}, \mathbf{R})$ for $\mathbf{R} = (X, Y, Z=0)$ as defined by Eq. (24) (in the noncomputationally intensive variant so that $\mathbf{R} = \mathbf{R}'$). The singular-value spectrum of the data matrix associated with the simulation in Fig. 5 is shown in Fig. 6(a). In this spectrum, the values of the first four singular values (arranged as a nonincreasing sequence so that $\sigma_1 \geq \sigma_2 \geq \sigma_3 \dots$) are clearly much higher than the rest, corresponding to indices >4 . Thus it is natural to interpret the first four singular values (and their singular functions) as corresponding to the signal subspace \mathcal{S}_y arising in the theory, and to associate the remaining singular values (and their singular functions) with the orthogonal complement or noise subspace \mathcal{S}_y^\perp . This behavior is to be expected from our theoretical development (Section 3), which shows that the dimensionality of the signal subspace for point targets is M^2 where M is the number of targets. In particular, in the present case, $M=2$ so that the signal subspace has dimensionality $M^2=4$, which is what one gathers from the spectrum in Fig. 6(a) that reveals only four dominant singular values.

The other singular values are theoretically zero in the absence of noise. Their very small (almost zero) values in

Fig. 6(a) are only the result of the numerical nature of the calculations, which gives rise to numerical roundoff and other minor errors and are manifested as numerical “noise”, as is well known. Therefore, we conclude that the dimensionality of the signal subspace is $M^2=4$, in agreement with our analysis in Section 3.

Next, Fig. 7 shows the respective pseudospectrum image under “single-snapshot” 20 dB SNR additive white Gaussian noise. Slices of the respective pseudospectrum $A(\mathbf{R}, \mathbf{R})$, where $\mathbf{R}=(X, Y, Z)$ for this 20 dB SNR case with different values of Z are shown in Fig. 8, where clearly the plot for the correct target plane ($Z=0$) exhibits the highest values of the pseudospectrum as well as the sharpest resolution, as expected. The corresponding singular value spectrum under 20 dB SNR is shown in Fig. 6(b). By comparing the spectra in Figs. 6(a) and 6(b), the most salient change from the noiseless condition [Fig. 6(a)] to the 20 dB SNR case [Fig. 6(b)] is in the level of the singular values that belong to the noise subspace (hence the terminology “noise subspace”).

Figures 7 and 8 thus show that, for the 20 dB SNR noise level, the pseudospectrum peaks at the correct scatterer positions, as desired. Nevertheless, it was also noted that as the scatterers’ distance diminishes, the resolution ability of the noncomputationally intensive pseudospectrum also diminishes, and that, in particular, there appears to be an approximate critical distance, for a given noise level, at which spurious peaks of the pseudospectrum begin to seriously limit the scatterer location estimation accuracy of this imaging procedure.

To explore comparatively the change in resolution versus noise level for the given remote sensing system and scatterers, we developed plots of the respective resolution versus SNR for three different methods: (a) the noncomputationally intensive intensity-only MUSIC method of this paper, (b) the computationally intensive intensity-

only signal-subspace-based method of this paper, and (c) the time-reversal MUSIC method in [14–18] under the assumption that one can measure *both* intensity and phase. The scatterers’ positions for these experiments were $\mathbf{X}_1=(X_1, Y_1, Z_1)=(5-\Delta/2, 5, 0)$ and $\mathbf{X}_2=(X_2, Y_2, Z_2)=(5+\Delta/2, 5, 0)$, where Δ is the target separation (in λ units). The probing aperture was maintained as in Fig. 4 for the methods applied in (a) and (b). For the method in (c) the probing aperture was reduced to 36 receivers and 36 transmitters.

The results are given in Fig. 9. One notes that, for all the imaging methods considered, the resolution improves exponentially as SNR increases. Of importance, and as expected, the computationally intensive intensity-only method outperforms the corresponding nonintensive method, while the imaging approach using both intensity and phase information clearly outperforms the intensity-only approaches even though the number of receivers and transmitters was reduced to about 30% in this last method. Clearly the resolution of the intensity-only methods in (a) and (b) is severely affected by the lack of phase information. Yet, for both methods there is a critical SNR value above which the resolution is subwavelength, and both methods enable perfect reconstruction in the absence of noise, as desired.

Figure 10 illustrates the pseudospectrum image for another simulation experiment aimed at addressing the smaller target separation of 3λ . In particular, in this experiment we selected the scatterers’ positions of $\mathbf{X}_1=(X_1, Y_1, Z_1)=(3.5, 5, 0)$ and $\mathbf{X}_2=(X_2, Y_2, Z_2)=(6.5, 5, 0)$ while maintaining the setup in Fig. 4. In particular, the probing aperture was kept as in Fig. 4 at the plane defined by $Z=15$, and $\tau_1=\tau_2=1$. Figure 10 shows slices of the noncomputationally intensive pseudospectrum under 24 dB SNR. The plot shows the pseudospectrum $A[\mathbf{R}=(X, Y, Z), \mathbf{R}]$ for different values of Z . It is seen that the

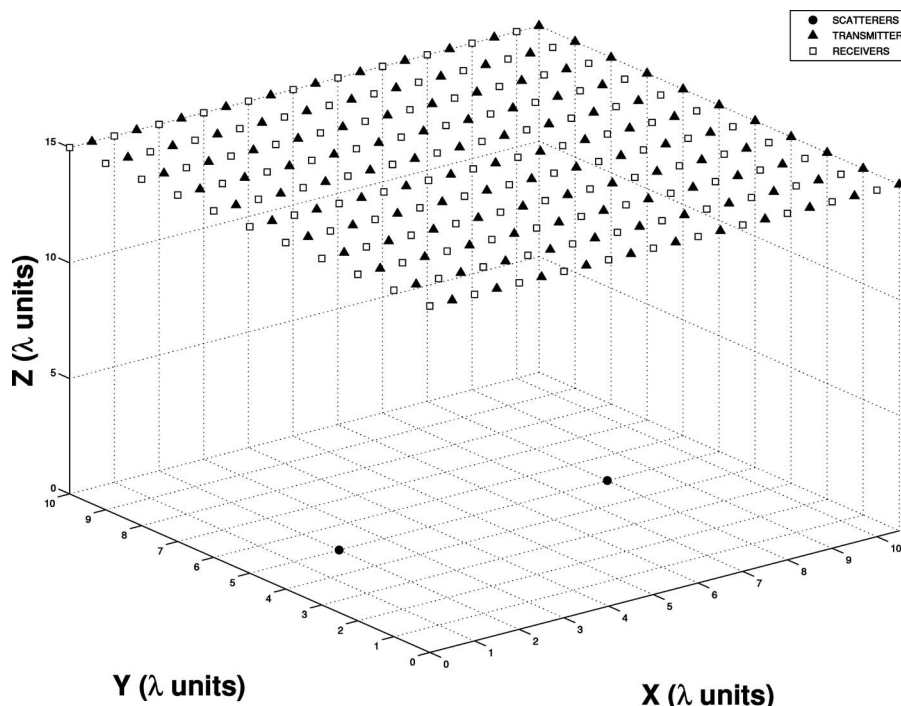


Fig. 4. Geometry for the first set of pointlike scatterer simulations.

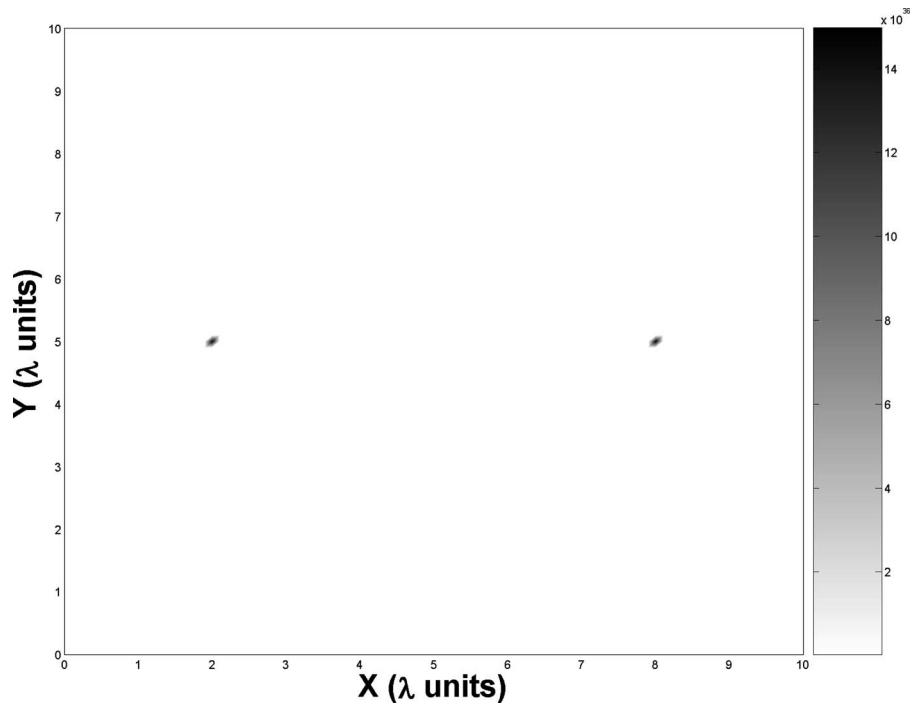


Fig. 5. Intensity-only pseudospectrum image of the two point targets under perfect data conditions (121 experiments).

scatterer locations are sharply resolved for the correct target plane ($Z=0$), as desired.

Next we illustrate in Fig. 11 far-field imaging of the two scatterers by the computationally intensive signal-subspace-based method. It is important to note that—as is easy to show by using the far-field approximation $G(\mathbf{r} \equiv r\hat{\mathbf{r}}, \mathbf{r}') \approx \exp(ikr - ik\hat{\mathbf{r}} \cdot \mathbf{r}')/4\pi r$ in the theory in Section 3—in the far-field case only the intensive version of the scatterer localization methodology derived in the paper applies. In particular, in the far field, the nonintensive method does not apply, and only the intensive form remains applicable.

The following results correspond to the geometry in Fig. 4 but with the aperture plane at $Z=200$ instead of at $Z=15$. The target parameters remain the same as in Fig. 4 for this simulation (thus the target separation remains 6λ). Figure 11 corresponds to the computationally intensive pseudospectrum $A_p[\mathbf{R}=(X,Y,Z=0)]$, which clearly reveals the correct target positions. Clearly the pseudospectrum has a smoother variation (smaller resolution) than in the near field. For instance, it has relatively large value in the vicinity of the line between the two target positions. Yet the highest values (peaks) occur at the correct target positions, as desired. However, the method was

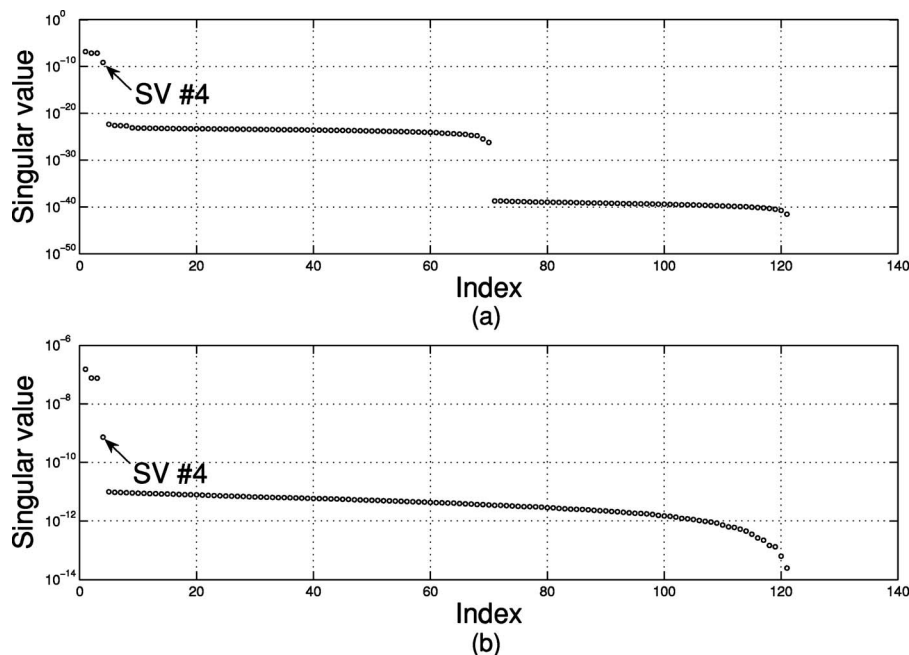


Fig. 6. Singular values of the data matrix for the case of two pointlike scatterers under (a) noiseless conditions and (b) 20 dB SNR.

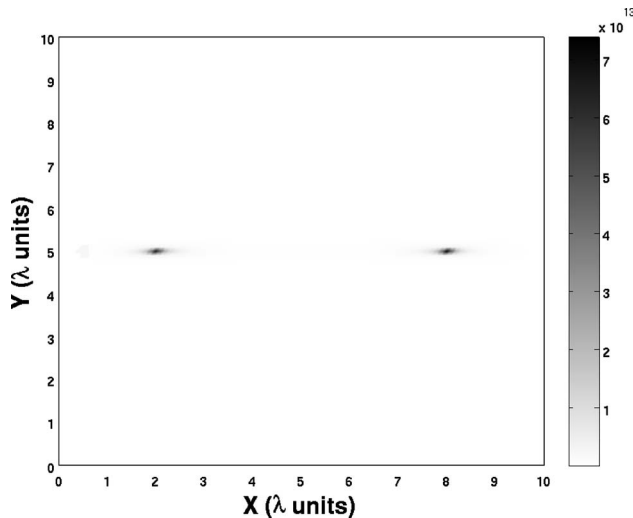


Fig. 7. Intensity-only pseudospectrum image of the two point targets under 20 dB SNR (121 experiments).

found to be very sensitive to mild noise levels in this particular example, which is not surprising since one should expect the associated combination of both limited-view and far-field factors to seriously limit the intrinsic resolution ability.

We have performed further simulations aimed at illustrating intensity-only imaging of more than two point targets. Two such examples, for four and six scatterers, are briefly discussed next. We consider first imaging of four unit-scattering-strength scatterers ($\tau_m=1, m=1, 2, 3, 4$) located at positions $\mathbf{X}_1=(X_1, Y_1, Z_1)=(5, 2, 1)$, that is, the plane where $Z=1$; $\mathbf{X}_2=(X_2, Y_2, Z_2)=(2, 3, 0)$; \mathbf{X}_3

$= (X_3, Y_3, Z_3)=(8, 3, 0)$; and $\mathbf{X}_4=(X_4, Y_4, Z_4)=(5, 7, 0)$, which corresponds to the plane where $Z=0$. Thus this configuration corresponds to one target located at the plane $Z=1$ with three additional targets located at plane $Z=0$. The probing aperture is located at the plane $Z=15$ as in Fig. 4.

Figure 12 illustrates the slices of the respective pseudospectrum image under 50 dB SNR for different values of Z . We can observe clearly that the sharpest and highest-valued images showing the correct scatterer positions correspond to the planes $Z=1$ and $Z=0$, as expected. The corresponding singular values are plotted in Fig. 13(b). Furthermore, the singular values of the noiseless condition have been plotted for comparison in Fig. 13(a). In this case $M=4$ so that, theoretically, the dimensionality of the signal subspace is expected to be $M^2=16$. The noiseless singular-value spectrum in Fig. 13(a) highlights the first 16 singular values as being of much larger magnitude than the rest (corresponding to the associated noise subspace). In Fig. 13(b), due to the added noise, the 16th singular value is clearly closer to the 17th singular value. The singular values whose values have changed more notably from Fig. 13(a) to Fig. 13(b) are the ones for index ≥ 17 (the noise subspace). It thus appears that, within computational error, these plots exhibit the behavior expected from the theory for point targets derived in Section 3.

Consider next six unit-scattering-strength targets located at positions $\mathbf{X}_1=(X_1, Y_1, Z_1)=(2, 6, 1)$, $\mathbf{X}_2=(X_2, Y_2, Z_2)=(8, 6, 1)$, $\mathbf{X}_3=(X_3, Y_3, Z_3)=(5, 2, 1)$, $\mathbf{X}_4=(X_4, Y_4, Z_4)=(2, 3, 0)$, $\mathbf{X}_5=(X_5, Y_5, Z_5)=(8, 3, 0)$, and $\mathbf{X}_6=(X_6, Y_6, Z_6)=(5, 7, 0)$, so that this configuration corresponds to three targets at plane $Z=1$ with three addi-

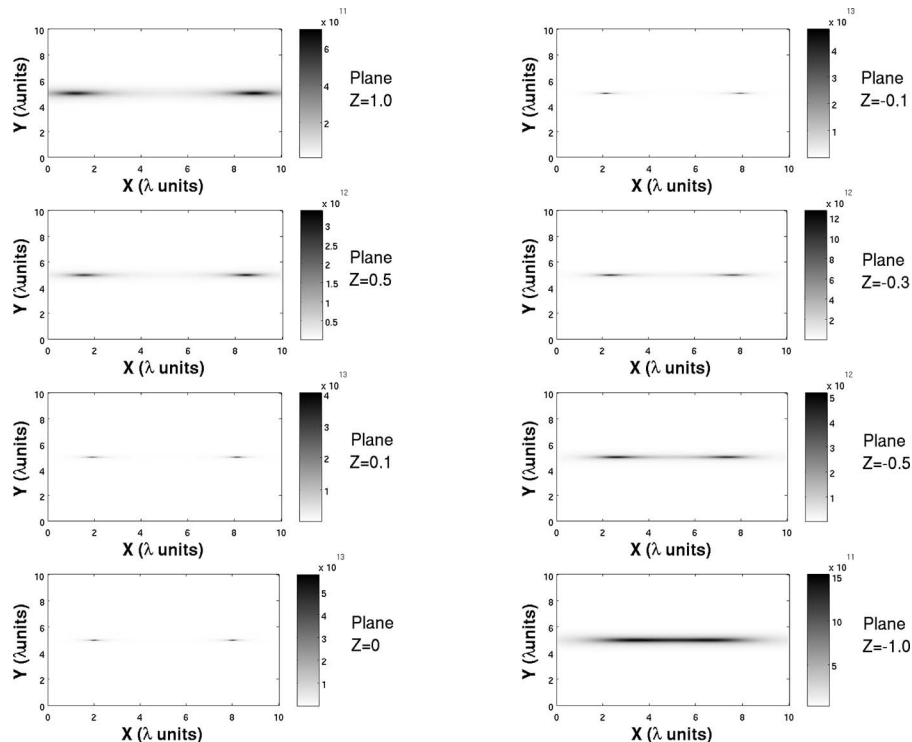


Fig. 8. Slices of the pseudospectrum $A[\mathbf{R}=(X, Y, Z), \mathbf{R}]$ under 20 dB SNR corresponding to different values of Z (different constant- Z planes).

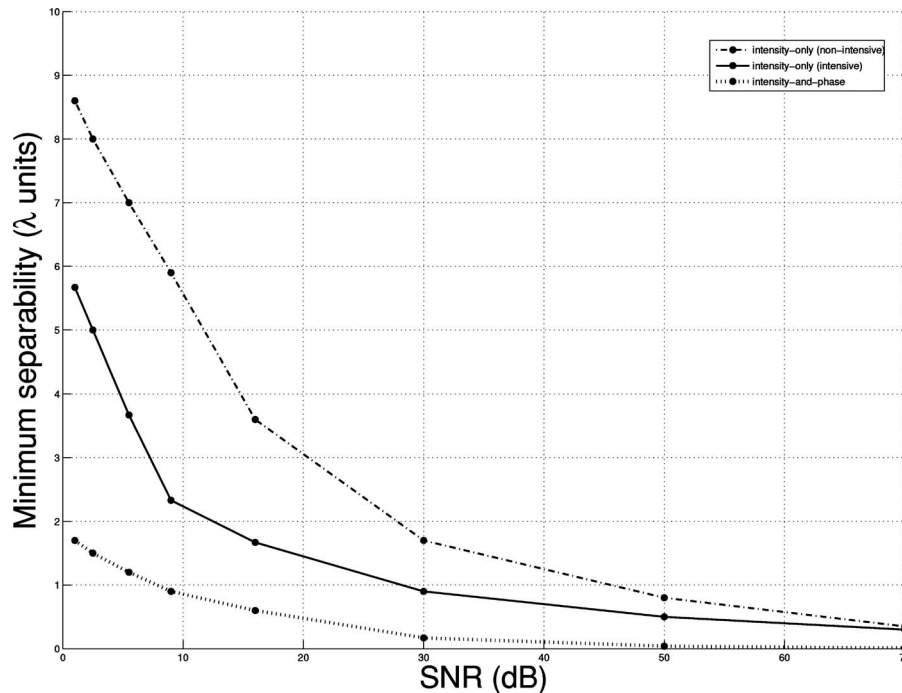


Fig. 9. Minimum target separability (resolution) versus SNR of intensity-and-phase versus intensity-only data conditions, where the latter involves the two variants (intensive and non-intensive). The upper curve corresponds to the case of intensity-only imaging via the noncomputationally intensive signal-subspace-based method of this paper. The middle curve corresponds to the case of intensity-only imaging via the computationally intensive signal-subspace-based method of this paper. As expected, the computationally intensive version of the method outperforms its nonintensive counterpart. Finally, the lower curve corresponds to the case of time-reversal MUSIC imaging using both amplitude and phase data. As expected, it clearly performs better than the approaches based on intensity-only data.

tional targets at plane $Z=0$. Again, the probing aperture is located at the plane where $Z=15$ as in Fig. 4. Figure 14 shows the slices of the respective pseudospectrum image under 50 dB SNR for different values of Z . The planes $Z=1$ and $Z=0$ exhibit the sharpest resolution and highest

values of the pseudospectrum, thereby correctly revealing the scatterer positions. The corresponding singular values are plotted in Fig. 15(b) along with the respective singular-value spectrum under noiseless conditions in Fig. 15(a). Once again, one notes that in this case, for

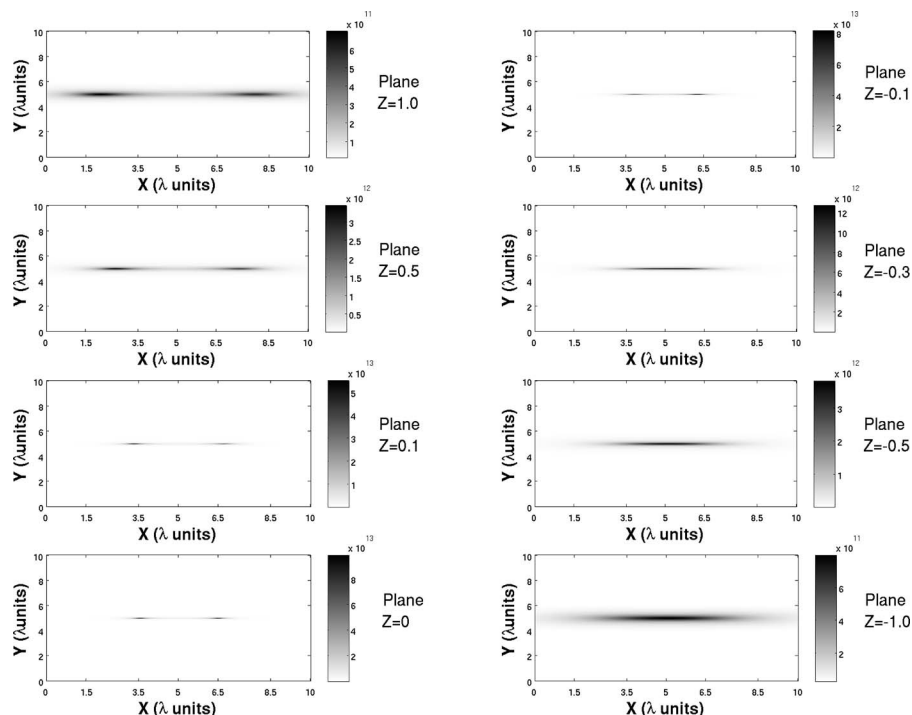


Fig. 10. Slices of the pseudospectrum $A[\mathbf{R}=(X, Y, Z), \mathbf{R}]$ for a second example under 24 dB SNR corresponding to different values of Z (different constant- Z planes).

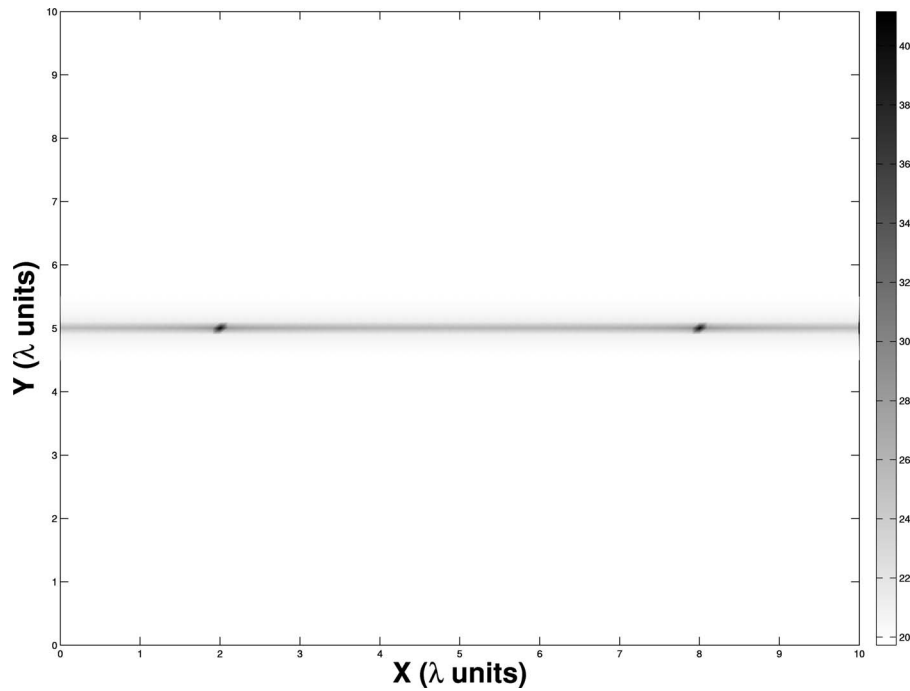


Fig. 11. Pseudospectrum $A_p[\mathbf{R}=(X,Y,Z=0)]$ with far-field data gathered by placing the aperture in the same configuration as in Fig. 4 but with the aperture plane at $Z=200$ instead of at $Z=15$ (121 experiments). The peaks in the image correspond to the correct target positions, as desired.

which $M=6$, the dimensionality of the signal subspace appears to be $M^2=36$, in agreement with the derived imaging theory for point targets.

We conclude this section with a canonical example illustrating the approximate intensity-only signal-subspace-based imaging for nonpointlike scatterers hav-

ing further spatial structure (shape), as discussed in Section 4. The illustrated example consists of imaging at wavelength $\lambda=60$ of the scatterer shown in Fig. 16, which has the shape of a square loop and whose scattering potential within this scatterer region is chosen to be unity (corresponding to a pure dielectric object). The simulated

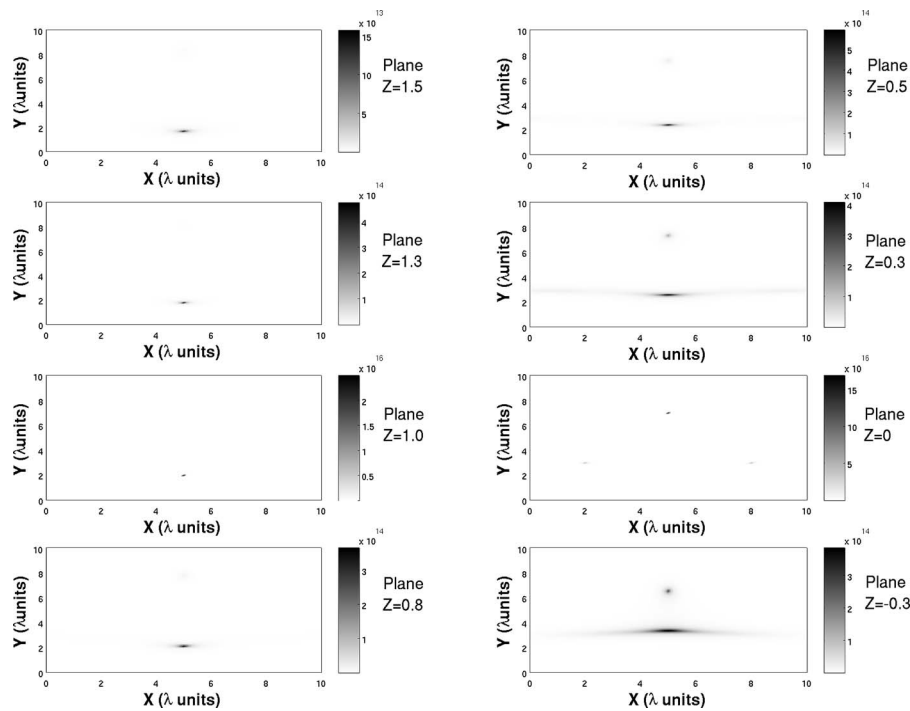


Fig. 12. Slices of the pseudospectrum $A[\mathbf{R}=(X,Y,Z),\mathbf{R}]$ for a four-pointlike-scatterers case where the scatterers' positions have been divided between two different planes: one target is located at plane $Z=1.0$ and three additional targets at plane $Z=0$ under 50 dB SNR. The slices correspond to different values of Z (different constant- Z planes).

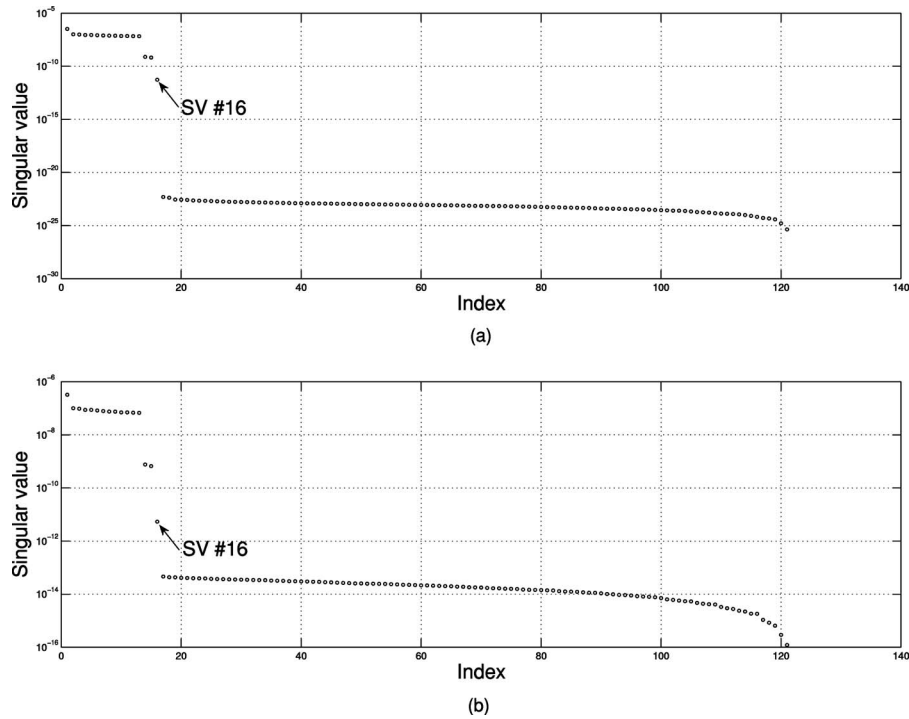


Fig. 13. Singular values of the data matrix for the case of four point-like scatterers under (a) noiseless conditions and (b) 50 dB SNR.

data were obtained by the Foldy–Lax multiple scattering model applied to a computational grid that was different from the grid employed later in the inversion to avoid the so-called “inverse crime” (see also [23] for a detailed description of this computational approach).

The idea is to illustrate superresolving imaging capabilities of the derived intensity-only signal-subspace-based imaging. In selecting the approximate signal versus

null subspaces from the data matrix, we adopted a methodology analogous to the L curve method, see, e.g., [23,33]. The square imaging array is formed by $25 \times 25 = 625$, 1.4-units-of-length-separated point transmitters (point sources) and receivers (photodetectors) (thus $N_T = 625$ and $N_R = 625$). The nonintensive extended target pseudospectrum $A[\mathbf{R}=(X,Y,Z),\mathbf{R}]$ in Eq. (28) is illustrated for different values of Z in Fig. 17 under perfect

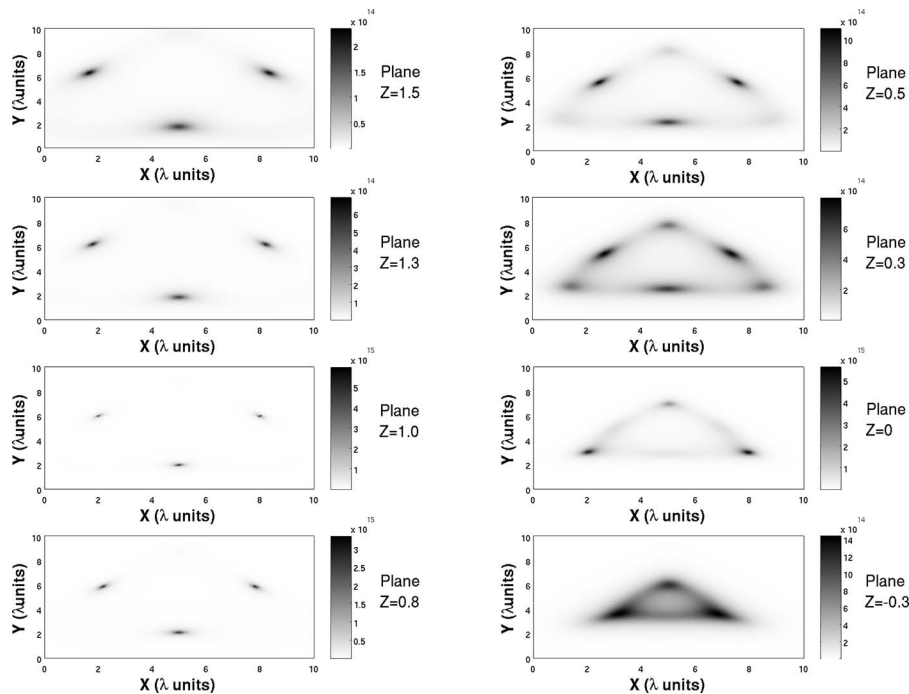


Fig. 14. Slices of the pseudospectrum $A[\mathbf{R}=(X,Y,Z),\mathbf{R}]$ for a six-pointlike scatterers case where the scatterers’ positions have been divided between two different planes ($Z=1.0, Z=0$) containing an equal number of scatterers under 50 dB SNR. The slices correspond to different values of Z (different constant- Z planes).

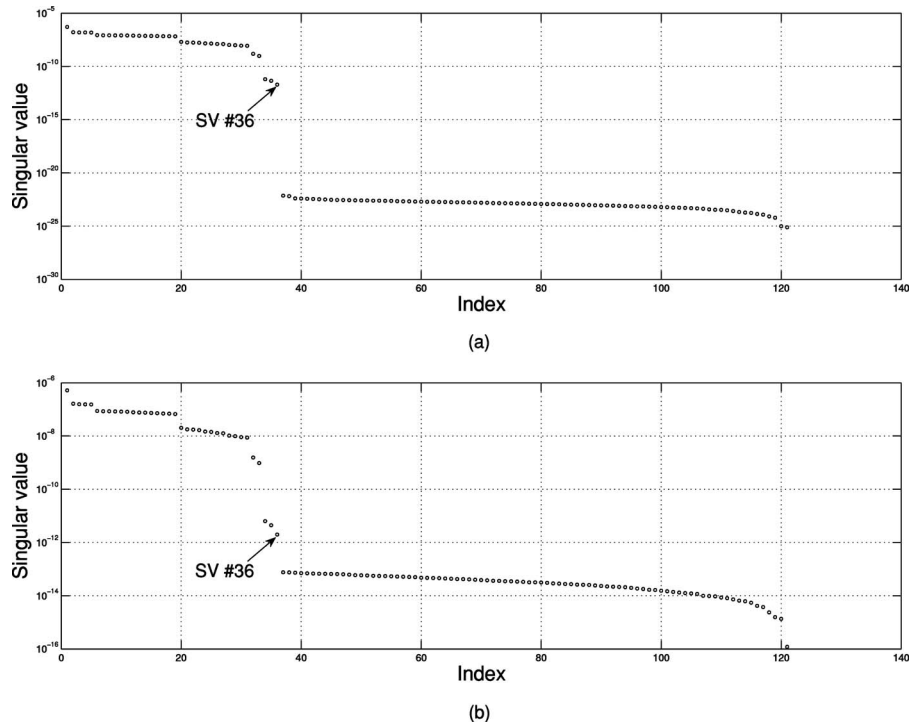


Fig. 15. Singular values of the data matrix for the case of six pointlike scatterers under (a) noiseless conditions and (b) 50 dB SNR.

data conditions and in Fig. 18 for 50 dB SNR. The images obtained for the correct target plane of $Z=0$ sharply reveal the square-loop scatterer, as desired. In addition, we have incorporated the respective singular-value spectra under noiseless condition [Fig. 19(a)] and 50 dB SNR [Fig. 19(b)]. In these simulations, the cutoff singular-value index has been estimated from the first knee in the log-scale singular-value spectrum of the data matrix. As highlighted in Fig. 19 in the noise-free case, the cutoff corre-

sponds to the 90th singular value, while in the noisy case, the cutoff corresponds to the 26th singular value.

Finally, we wish to mention that during the development of the research reported in this paper we ran several other near-field and far-field examples such as different numbers of pointlike scatterers (between two and eight) being interrogated by both coincident and noncoincident transmit and receive apertures, as well as other extended scatterers such as a basic linear scatterer and a (filled)

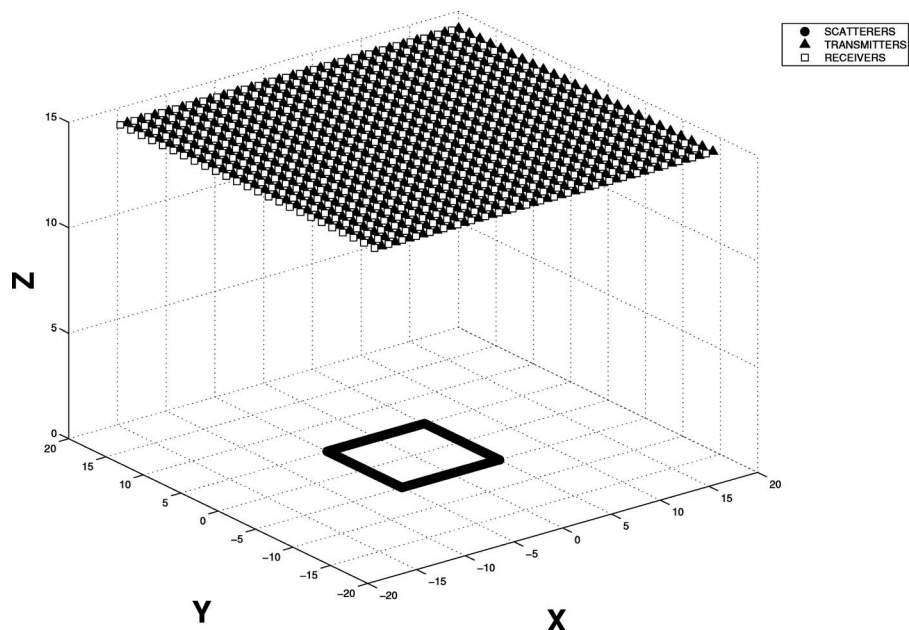


Fig. 16. Imaging array formed by $25 \times 25 = 625$ elements and a square-loop scatterer whose shape we wish to deduce from scattered field intensity measurements at the array.

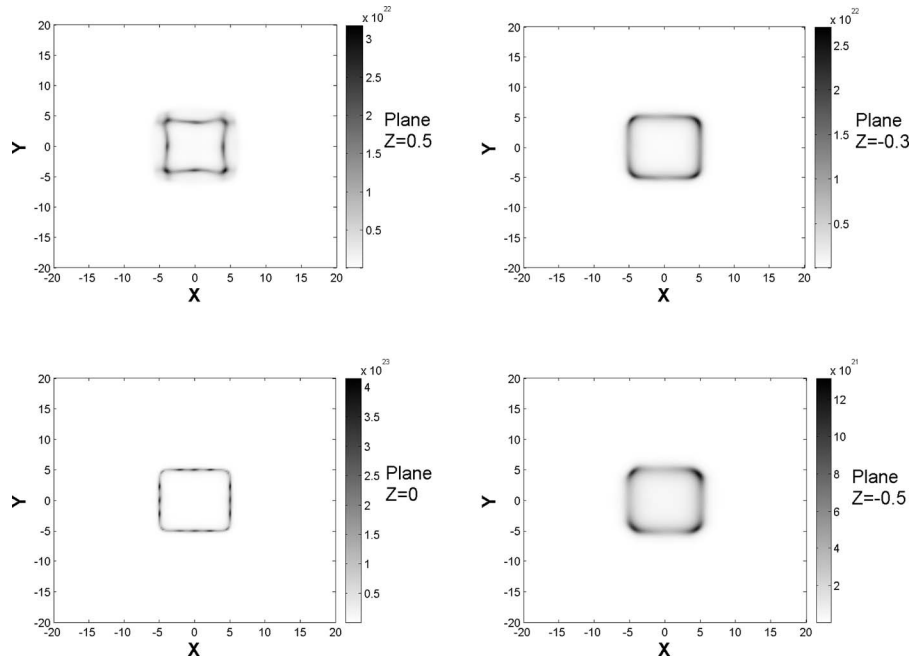


Fig. 17. Intensity-only pseudospectrum image for the square-loop scatterer under perfect data conditions. The sharpest image corresponds to the correct target plane of $Z=0$, as desired.

square plate target. The cases considered incorporated noiseless conditions as well as distinct values of SNR, and further validated the derived signal-subspace-based theory and methodology for intensity-only imaging established in the paper.

6. CONCLUSION

We have developed a theory and methodology for intensity-only signal-subspace-based imaging of both small (pointlike) and more general nonpointlike scatter-

ers having spatial structure (shape), that was motivated by optical applications in which field phase information is not available. Clearly the lack of field phase information affects the reconstructions relative to the case where both field amplitude and phase are available. For instance, the method requires a higher minimal number of sensors than the amplitude-and-phase counterpart (as we showed in the theoretical discussion) and is also more sensitive to noise (as we discussed with a canonical two-point-target example in the computer simulations Section 5). But this is the realistic situation in the optical regime wherein re-

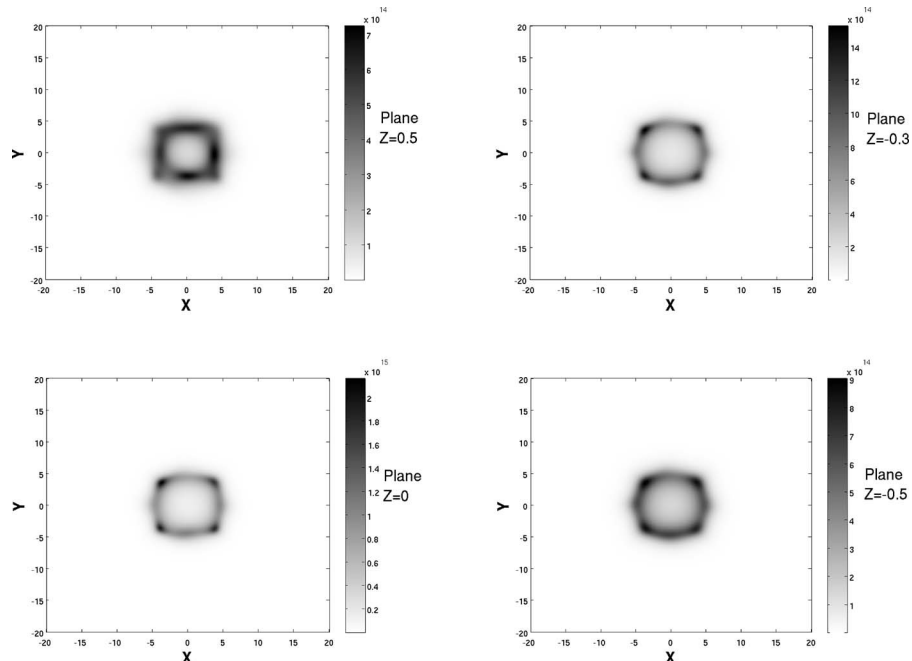


Fig. 18. Intensity-only pseudospectrum image for the square-loop scatterer under 50 dB SNR. The sharpest image corresponds to the correct target plane of $Z=0$, as desired.

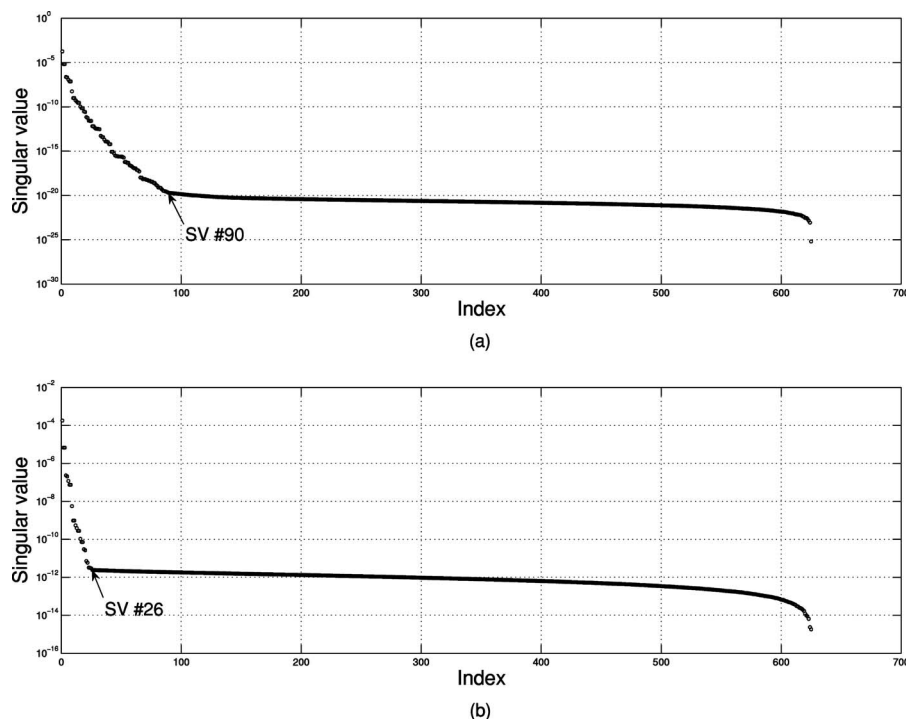


Fig. 19. Singular values of the data matrix for the case of the square-loop scatterer under (a) noiseless conditions and (b) 50 dB SNR.

ceivers (photodetectors) measure only field intensity. Thus the problem is both practically motivated and important, since this limitation must be coped with in practical optical imaging.

The proposed approach is a natural extension of the time-reversal MUSIC method to the intensity-only (nonfield-phase information) regime. It is based on a clever linearization of the problem by the consideration not of the original induced sources (due to the incident excitation fields) but of another source function which still holds information about the scatterer's support. The derived intensity-only signal-subspace-based imaging principle has been illustrated with the aid of canonical numerical examples.

Future directions include further simulations considering realistic conditions (using as reference commercially available digital cameras), detailed Cramér–Rao bound calculations as pertains to the intensity-only conditions, and further comparative analysis relative to the more familiar full-phase information case. Finally, we also plan to examine the possibility of embedding the scatterers in other scatterers which can be known *a priori*, such as ground planes, metamaterials, or other, to enhance both the intrinsic imaging capabilities and the particular performance of the intensity-only signal-subspace-based imaging method derived in this work. Such helper-embedding media can create multiple scattering interaction with the sought-after scatterer, helping to extract evanescent plane-wave spectral components of the scatterer's field, thereby facilitating better-resolved images. We plan to investigate these and related ideas in the future.

ACKNOWLEDGMENTS

This work was supported by the United States Air Force Office of Scientific Research under grant FA9550-06-01-

0013, and is affiliated with the Gordon Center for Subsurface Sensing and Imaging Systems, under the Engineering Research Centers Program of the National Science Foundation (award EEC-9986821). The authors wish to thank the reviewers for constructive comments that enhanced this work.

REFERENCES

1. G. Gbur and E. Wolf, "Diffraction tomography without phase information," *Opt. Lett.* **27**, 1890–1892 (2002).
2. G. Gbur and E. Wolf, "The information content of the scattered intensity in diffraction tomography," *Inf. Sci. (N.Y.)* **162**, 3–20 (2004).
3. G. Gbur and E. Wolf, "Hybrid diffraction tomography without phase information," *J. Opt. Soc. Am. A* **19**, 2194–2202 (2002).
4. G. Gbur, M. A. Anastasio, Y. Huang, and D. Shi, "Spherical-wave intensity diffraction tomography," *J. Opt. Soc. Am. A* **22**, 230–238 (2005).
5. M. A. Anastasio, D. Shi, Y. Huang, and G. Gbur, "Image reconstruction in spherical-wave intensity diffraction tomography," *J. Opt. Soc. Am. A* **22**, 2651–2661 (2005).
6. A. J. Devaney, "Diffraction tomographic reconstruction from intensity data," *IEEE Trans. Image Process.* **1**, 221–228 (1992).
7. M. H. Maleki, A. J. Devaney, and A. Schatzberg, "Tomographic reconstruction from optical scattered intensities," *J. Opt. Soc. Am. A* **10**, 1356–1363 (1992).
8. M. H. Maleki and A. J. Devaney, "Phase retrieval and intensity-only reconstruction algorithms for optical diffraction tomography," *J. Opt. Soc. Am. A* **10**, 1086–1092 (1993).
9. O. M. Bucci, L. Crocco, M. D'Urso, and T. Isernia, "Inverse scattering from phaseless measurements of the total field on open lines," *J. Opt. Soc. Am. A* **23**, 2566–2577 (2006).
10. L. Crocco, M. D'Urso, and T. Isernia, "Inverse scattering from phaseless measurements of the total field on a closed curve," *J. Opt. Soc. Am. A* **21**, 622–631 (2004).
11. A. Litman and K. Belkebir, "Two-dimensional inverse profiling problem using phaseless data," *J. Opt. Soc. Am. A* **23**, 2737–2746 (2006).

12. T. Takenaka, D. J. N. Wall, H. Harada, and M. Tanaka, "Reconstruction algorithm of the refractive index of a cylindrical object from the intensity measurements of the total field," *Microwave Opt. Technol. Lett.* **14**, 182–188 (1997).
13. S. Caorsi, A. Massa, M. Pastorino, and A. Randazzo, "Electromagnetic detection of dielectric scatterers using phaseless synthetic and real data and the memetic algorithm," *IEEE Trans. Geosci. Remote Sens.* **41**, 2745–2753 (2003).
14. H. Lev-Ari and A. J. Devaney, "The time-reversal technique re-interpreted: Subspace-based signal processing for multi-static target location," *Proc. of the 2000 IEEE Sensor Array and Multichannel Signal Processing Workshop* (IEEE, 2000)509–513.
15. C. Prada and J. L. Thomas, "Experimental subwavelength localization of scatterers by decomposition of the time reversal operator interpreted as a covariance matrix," *J. Acoust. Soc. Am.* **114**, 235–243 (2003).
16. S. K. Lehman and A. J. Devaney, "Transmission mode time-reversal super-resolution imaging," *J. Acoust. Soc. Am.* **113**, 2742–2753 (2004).
17. F. K. Gruber, E. A. Marengo, and A. J. Devaney, "Time-reversal imaging with multiple signal classification considering multiple scattering between the targets," *J. Acoust. Soc. Am.* **115**, 3042–3047 (2004).
18. A. J. Devaney, E. A. Marengo, and F. K. Gruber, "Time-reversal-based imaging and inverse scattering of multiply scattering point targets," *J. Acoust. Soc. Am.* **118**, 3129–3138 (2005).
19. A. Kirsch, "The MUSIC algorithm and the factorization method in inverse scattering theory for inhomogeneous media," *Inverse Probl.* **18**, 1025–1040 (2002).
20. S. Hou, K. Solna, and H. Zhao, "Imaging of location and geometry for extended targets using the response matrix," *J. Comput. Phys.* **199**, 317–338 (2004).
21. S. Hou, K. Solna, and H. Zhao, "A direct imaging algorithm for extended targets," *Inverse Probl.* **22**, 1151–1178 (2006).
22. S. Hou, K. Solna, and H. Zhao, "A direct imaging method using far field data," *Inverse Probl.* **23**, 1533–1546 (2007).
23. E. A. Marengo, F. K. Gruber, and F. Simonetti, "Time-reversal MUSIC imaging of extended targets," *IEEE Trans. Image Process.* **16**, 1967–1984 (2007).
24. F. Cakoni and D. Colton, *Qualitative Methods in Inverse Scattering Theory* (Springer, 2006).
25. R. Potthast, *Point Sources and Multipoles in Inverse Scattering Theory* (Chapman & Hall/CRC, 2001).
26. R. O. Schmidt, "Multiple emitter location and signal parameter estimation," *IEEE Trans. Antennas Propag.* **34**, 276–280 (1986).
27. C. W. Therrien, *Discrete Random Signals and Statistical Signal Processing* (Prentice Hall, 1992).
28. E. A. Marengo and F. K. Gruber, "Subspace-based localization and inverse scattering of multiply scattering point targets," *EURASIP J. Advances in Signal Processing* **2007**, 17342, 16 pp. (2007).
29. J. H. Taylor, *Scattering Theory* (Wiley, 1972).
30. R. Pierri and A. Tamburrino, "On the local minima problem in conductivity imaging via a quadratic approach," *Inverse Probl.* **13**, 1547–1568 (1997).
31. D. Colton and R. Kress, *Integral Equation Methods in Scattering Theory* (Wiley, 1983).
32. A. J. Devaney, "Super-resolution processing of multi-static data using time-reversal and MUSIC," Northeastern University, 2000-year report available at <http://www.ece.neu.edu/faculty/devaney/ajd/preprints.htm>.
33. M. Bertero and P. Boccacci, *Introduction to Inverse Problems in Imaging* (Institute of Physics, 1998).
34. R. Pierri and F. Soldovieri, "On the information content of the radiated fields in the near zone over bounded domains," *Inverse Probl.* **14**, 321–337 (1998).
35. D. A. B. Miller, "Communicating with waves between volumes: evaluating orthogonal spatial channels and limits on coupling strengths," *Appl. Opt.* **39**, 1681–1699 (2000).
36. P. C. Hansen, *Rank Deficient and Ill-Posed Problems: Numerical Aspects of Linear Inversion* (SIAM, 1998).
37. M. Tanter, J.-L. Thomas, and M. Fink, "Time reversal and the inverse filter," *J. Acoust. Soc. Am.* **108**, 223–234 (2000).
38. E. A. Marengo, "Further theoretical considerations for time-reversal MUSIC imaging of extended scatterers," invited paper, in *IEEE Statistical Signal Processing Workshop 2007*, Madison, Wisconsin, USA (IEEE, 2007), pp. 304–306. ISBN: 978–1–4244–1198–6.
39. L. L. Foldy, "The multiple scattering of waves: I. General theory of isotropic scattering by randomly distributed scatterers," *Phys. Rev.* **67**, 107–119 (1945).
40. M. Lax, "Multiple scattering of waves," *Rev. Mod. Phys.* **23**, 287–310 (1951).
41. A. Ishimaru, *Wave Propagation and Scattering in Random Media* (IEEE Press, 1997).
42. L. Tsang, J. A. Kong, K.-H. Ding, and C. O. Ao, *Scattering of Electromagnetic Waves: Numerical Simulations* (Wiley, 2001).
43. R. K. Snieder and J. A. Scales, "Time-reversed imaging as a diagnostic of wave and particle chaos," *Phys. Rev. E* **58**, 5668–5675 (1998).
44. E. A. Marengo and F. K. Gruber, "Non-iterative analytical formula for inverse scattering of multiply scattering point targets," *J. Acoust. Soc. Am.* **120**, 3782–3788 (2006).